Multiphoton Fabrication of Proteinaceous Nanocomposite Microstructures with Photothermal Activity in the Infrared.

A. Zeynali[1], M. Marini[1], G. Chirico,[1,2,,4,] M. Bouzin[1], M. Borzenkov[1,4], L. Sironi[1], L. D'Alfonso[1], P. Pallavicini[3], V. Cassina[4], F. Mantegazza,[4] F. Granucci,[6,7] L. Marongiu,[6,7] D. Polli,[5] A. De La Cadena Perez[5], M. Collini.[1,2,4]*

1, Department of Physics, University of Milano-Bicocca, Piazza della Scienza 3, 20126 Milano (I)

2, CNR Institute for Applied Science and Intelligent Systems, Via Campi Flegrei 34, 80078, Pozzuoli (I).

3, Department of Chemistry, University of Pavia, Via Taramelli 12, 27100, Pavia (I)

4, Department of Medicine and surgery, Nanomedicine Center, University of Milano-Bicocca, Via Follerau, 3 - 20854 Vedano al lambro (I)

5, Department of Physics, Politecnico di Milano, Piazza Leonardo 32, 20133, Milano (I)

6, Department of Bioscience, University of Milano-Bicocca, Piazza della Scienza 2, 2016 Milano (I)

7, INGM, National Institute of Molecular Genetics "Romeo ed Enrica Invernizzi", Milan, Italy.

Abstract.

Two-photon laser writing is used here to fabricate 3D proteinaceous microstructures with photothermal functionality in the near infrared spectral region and tunable elasticity. The photo-cross-linking is initiated in Bovine Serum Albumine (BSA) by Rose Bengal or Methylene Blue and the photo-thermal effect arises from gold non-spherically symmetric nanoparticles dispersed in the ink. Massive energy transfer of the plasmonic resonances of the gold nanoparticles to Methylene Blue prevents effective photo-crosslinking of BSA. However, stable microstructures with photo-thermal functionality can be fabricated in the Rose Bengal proteinaceous inks. On these microstructures, with a gold atoms concentration as low as 1% w/w, a highly localized temperature increase can be quickly ($\cong 1\ s$) reached and maintained under continuous wave laser irradiation at 800 nm. The photothermal efficiency under continuous wave laser irradiation depends on the thickness of the microstructure and can reach $12.2 \pm 0.4\ ^{o}C/W$. These proteinaceous microstructures represent therefore a promising platform for future applications in the fields like physical stimulation of cells for regenerative Nanomedicine.

Keywords: Femtosecond laser; Micro-fabrication; Laser Direct Writing; Two-photon absorption; cross-linking

Conflict of Interest: none of the authors have a financial/commercial Conflict of Interest.

1. Introduction

The advances in the fabrication of 3D[1,2] functional micro structures[3] is fostering applications in many fields.[4,5] Developments related to Medicine, like physical stimulation

of cells and tissue regeneration in general,[6] are particularly promising. Direct Laser Writing (DLW) of micro-structures of proteins[7-12] offers many advantages for biomedical applications, since it exploits photo-crosslinking[13-15] that occurs at low temperature and limits the damage to the chemical structure of the protein.[16] Two-photon excitation (TPE)[17,18] coupled to DLW allows to fabricate biocompatible nano-structures[9,15,19-24] down to a resolution of few tens of nanometers[25] in a single ink deposition, differently from stereo lithography,[26] ink-jet printing of hydrogel droplets[27] or laser-induced forward transfer.[28]. At the same time, the use of Near InfraRed (NIR) wavelengths (800nm – 1200nm) for TPE, further reduces the possible damage of the biological components of the ink.[29]

However, to endow the microstructures with physical functionalities is challenging since the addition of molecular or nano-components to the DLW ink affects the photo-crosslinking. This occurs either directly (route-1), when the triple state of a photo-initiatior (PI) reacts with proton donor moieties of the protein to produce initiating radicals,[14, 30] or indirectly (route-2),[31] when the energy from the excited PI creates singlet oxygen that oxidizes a protein amminoacid.

Functional microstructures can be obtained by post-writing coating with specific cellular receptors[32] or by dispersing functional compounds, like nanoparticles, in the LDW ink before printing.[33] Gold nanoparticles have limited toxicity[34] and feature Localized Surface Plasmon Resonances (LSPRs)[35] whose energy depends on size, shape and the surface dielectric constant,[36-40] falls in the Visible-NIR range and gives rise to a pronounced photo-thermal effect. These features have triggered a demand for gold-based polymer nanocomposites[3,41-43] to be applied as biosensors,[35,44] as flexible electronics,[45] in antibacterial treatment[46,47] or in artificial implants and for electrical or thermal stimulation of cells[48-50] also related to their pronounced photothermal activity.[51,52]

Microstructures containing gold nanoparticles have been obtained either by embedding preformed gold nanoparticles in resins containing a photo-initiator for TPE photo-crosslinking[53] or by simultaneous in-situ photo-synthesis of nanoparticles and photo-crosslinking of the monomers,[43,52,54] from synthetic resins, like SU-8[54] or PETA,[55] to PVA[52] or proteins,[21] mostly Bovine Serum Albumin (BSA). The addition of gold nanoparticles to the DLW ink allows to reduce the writing power and augment the writing resolution.[21] The simultaneous photo-crosslinking of monomers and photo-synthesis of gold nanoparticles offers some other advantages.[52,55,56] Palermo et al.[52] have developed PVA substrates in which spherical gold nanoparticles photo-synthesized in-situ endowed the microstructures with photo-thermal effect ranging from 6.8 to 45 $^{0}C/W$, when irradiated at 532 nm. However, this study was limited to the photo-synthesis of spherical nanoparticles that can be activated only in the visible part of the spectrum and to a synthetic polymer. To our knowledge, no study reported the possibility to fabricate proteinaceous microstructures with tunable photo-thermal effect in the near infrared part of the spectrum due to embedded non-spherically symmetric gold nanoparticles.

Our aim is to develop protein based microstructures with photo-thermal functionality in the NIR spectral region due to gold nanoparticles. The spatially confined heat loads could then be used, for example, to induce highly localized responses in cells [57-59] or for micro-pumps in microfluidics.[60,61] For this purpose, we need gold nanoparticles with high photothermal efficiency, typical of non-spherically symmetric or non uniform gold nanoparticles, like nano-branched nanoparticles,[62] nano-stars[51] or nanocages. Such nanoparticles cannot be obtained easily by in-situ photo-reduction of gold salts in a polymeric blend.[21,52,56] Our strategy is therefore to couple the preparation of stable suspensions of non-spherically symmetric gold nanoparticles in BSA at high nanoparticles concentration,[63] with an accurate choice of the photo-initiator and the writing conditions. For the first time, we give a full

characterization of the Photo-Thermal (PT) effect induced in proteinaceous microstructures of various thickness under pulsed and CW laser excitation as a function of the irradiation intensity. Our main result is high resolution proteinaceous microstructures endowed with efficient ($\cong$ 12 $^{o}C/_{W}$), spatially confined ($\cong 1-30\ \mu m$) and fast ($\cong 1\ s$ rising time) PT effect triggered by 800 nm light.

2. Results and Discussion

2.1 Microfabrication of Protein-based Structures.

2.1.1 *Choice of the photo-initiators for two-photon absorption.* Two photo-initiators were tested for our aim: Methylene Blue (**MB**, route2, type II),[64] a cationic dye that absorbs at 670 nm (**Figure 1A)** with very low fluorescence quantum yield $\Phi_F \cong 0.03$ (water)[65] and high singlet Oxygen generation yield $\Phi_\Delta \cong 0.57$,[65;66] and Rose Bengal (**RB**, route1, type I), an anionic dye that absorbs at 540 nm with a slightly higher fluorescence quantum yield, $\Phi_F \cong 0.11$[67] (**Figure 1B**).

In two-photon cross-linking,[14,68-70] the TPE of the photo-initiator is restricted to a small volume $V_{TPE} \cong 0.43\frac{\lambda^3}{NA^4}$, determined by the wavelength, λ, and the objective Numerical Aperture, NA, that determines also the laser spot size (radius) $\omega_0 \cong 0.61\ \frac{\lambda}{NA}$. The excitation rate, k_{TPE}, scales with the square of the average power, $\langle P \rangle$, the laser duty cycle, d_c, the second-order cross-section, σ_2, and the fourth power of the NA: $k_{TPE} \approx \frac{\sigma_2 <P>^2 NA^4}{((\pi hc\lambda)^2 d_c)}$. The TPE spectrum (600 nm – 1200 nm) follows the single-photon absorption one at approximately twice the single photon absorption wavelength (**Figure 1B**)[71-73] and falls typically in the range 720-850 nm.[53]

2.1.2. Two-photon absorption control. Patterns of different shapes (**Figure SI.1**) and thickness were photo-cross-linked in BSA inks by moving the sample on the microscope

stage. In our experimental condition ($750\ nm\ \leq \lambda \leq 810\ nm$), $V_{TPE} \cong 0.4\ fL$ and the beam spot size (1/e^2 radius) is $\omega_0 \cong 0.57\ \mu m$. Thin and thick structures were obtained, respectively, by photo-crosslinking a single layer of the ink (L1) or 5 consecutive layers (L5) at distance of $0.5\mu m$ along the optical axis. The nominal microstructure thickness is $\cong 1.3\ \mu m$ (L1) and $\cong 3.0\ \mu m$ (L5), as can be estimated from the Rayleigh range, $z_R = \frac{\pi\omega_0^2}{\lambda} \cong 1.3\ \mu m$.

The excitation wavelength and the type of photo-initiator affect the photo-crosslinking threshold power ($\langle P_{th} \rangle$ =minimum to reach the density of radicals needed to induce photo-crosslinking) and the writing threshold power ($\langle P \rangle_{write}$ = minimum to write a continuous protein-based micro-structure). The latter depends also on the laser scanning speed (1 µm/s - 10 µm/s). We measured $\langle P \rangle_{thr}$ as the minimum value for which a confined, optically denser, blob appeared in the ink. In order to write a continuous microstructure at a laser scanning speed v_{write}, we need to raise the power to a higher level $\langle P \rangle_{write} \geq \langle P \rangle_{thr}$. The corresponding energy, $E_{write} = \langle P \rangle_{write} \frac{\omega_0}{v_{write}}$, scales as (see **Figure SI.2**) $E_{write} \cong E_0 + \frac{B}{v_{write}}$.

2.1.3 Microfabrication of Protein-based Structures with cationic photo-initiator. For microfabrication in inks containing MB, Poly-Vinyl-Pyrrolidone (PVP) (10% w/w), BSA (300 mg mL^{-1}) and MB (70 μM) were dissolved in Milli-Q water. PVP allows to control the ink viscosity in a wide range of values (**Figure SI.3**). The ink was stable for up to 9 days in the fridge at 4 ^oC. Approximately 50µL of ink solution was drop-casted on circular chamber (8 mm diameter, 1 mm thickness) built on a pre-cleaned microscope cover-glass. The hydration of the ink was controlled by sealing it with a drop of immersion oil on the free surface. The written structure was then fixed and washed in Milli-Q water. Stimulated Raman microscopy images of the structure at the CH stretching frequency indicates that no residue of organic compounds lies outside the photo-cross-linked area after the washing procedure (**Figure SI.4**).

$\langle P \rangle_{thr}$ and $\langle P \rangle_{write}$ are practically constant (**Figure 1C**) over the range 750nm to 810nm, with a slight drop at 780nm, which is taken as the writing wavelength in the following experiments. At 780 nm, the writing threshold power for the MB ink at v_{write} =1 μm/s is $\langle P \rangle_{write}$= 29 $\pm$ 1 mW (**Figure 2D**).

Square arrays (L1) were written in the power range 10 $\leq$ $\langle P \rangle$ $\leq$ 90 mW and characterized first by confocal fluorescence imaging at the MB emission wavelength ($\lambda_{em} = 700 \pm 20\, nm$) (**Figure 2A, B**). At least for $\langle P \rangle \geq 30\, mW$, the Full Width at Half Maximum (FWHM) of the written lines scales linearly with the writing power (**Figure 2C**, slope = 7 $\pm$ 1.6$\frac{nm}{mW}$) probably due to the photo-thermal effect in the ink ($\Delta T \cong 8.5\ ^0C$ in the MB stock solution, irradiated at λ =800 nm, <P>= 160 mW). The minimum FWHM width estimated from **Figure 2C** is 1040 $\pm$ 120 nm for the writing power $< P >= 44\ \pm 4\, mW$. This value is approximately twice the diffraction limit spot size, $\omega_0 \cong 0.6\frac{\lambda}{NA} \cong 450\, nm$.

The thickness of the printed structures (<P> = 44 mW) evaluated by SEM (under vacuum, **Figure 3A**) and AFM (**Figure 3B, D**) are compared with the estimate made on fluorescence confocal images (**Figure 2A**) in **Table I**. The FWHM of the microstructured L1 lines ($\Omega \cong 1.17 \pm 0.05\, \mu m$) measured on the AFM images of square arrays agree well with those measured on the fluorescence confocal images. Slightly lower values, $\Omega \cong 0.94 \pm 0.04\, \mu m$ are measured on single lines. On the L5 lines, the width is larger due to the convolution of the microstructure profile with the AFM conical tip. The FWHM measured on the SEM images was instead $\cong 30\%$ lower, due to de-swelling of the microstructures dehydrated under vacuum.

The thickness of the L1 microstructures, measured on their AFM images, was uniform within 7% along the direction of writing (**Figure 3B**). However, at the crossings of square arrays (**Figure 3A**), larger thickness variations were observed, always downhill of the direction of the second axis tracing (circles in **Figure 3A**). This is probably due to the optical refraction

of the laser beam within the already cross-linked line (see **Figure SI.5**). In the L5 structures we measured a 30% increase in the lines thickness at the array crossings (**Figure 3D, E**) and a tiny harmonic modulation in the thickness of the written lines between the crossings, with a periodicity $1.5 \pm 0.05\ \mu m$ (**Figure 3C**, lower panel), very close to the size of the beam waist.

2.1.4 Young modulus of proteinaceous micro-structures written in inks based on a cationic photo-initiator. The Young modulus, E_{sample}, measured on DLW rectangular parallelepipeds written in the MB/BSA ink ([BSA] = 300 mg/mL) has a log-normal distribution (**Figure 4A**) with mode value, $E_{sample} = 240 \pm 80$ kPa, much smaller than that measured on the glass slide (170 nm thick), $E_{glass} = 6.9 \pm 2.1$ MPa. The E_{sample} value agrees with that of soft biological tissues[74] and biomimetic materials[75] and suggest that these structures could be used as a substrate for cell growing. Indeed, 4T1 cells (human breast cancer) grew for at least 24 hours on the proteinaceous microstructures with no evidence of cytotoxicity (**Figure SI.6**).

2.1.5 Microfabrication of Protein-based Structures with anionic photo-initiator. For microfabrication with a type I initiator, a stock solution of 50 mg/mL BSA, 2mM Rose Bengal (RB; **Figure1B**) was prepared (dye molecules per proteins ≅ 2.8). We investigated the DLW wavelength range 740-850 nm (**Figure 1D**) and swept the power from 10mW to 150mW (**Figure 2E**), building microstructures of increasing values of thickness ($1\mu m$ to $2.7\mu m$). Stable micro-structuring conditions could be obtained at writing speeds up to 10 $\mu m/s$, only in a narrow power range (100mW - 150mW; **Figure 2F**). Below 100 mW, the microstructures suffered from discontinuities. Above 150 mW and at low scanning rates, microbubbles prevented writing, and at scanning rates ≅ 10 $\frac{\mu m}{s}$, no stable microstructures could be written even though microbubbles were not forming. The quality of the written microstructures was assessed by fluorescence confocal imaging (**Figure 1D, Figure 2F**) of the RB dye in the microstructures (**Figure 2E**) and by SEM and AFM imaging (**Figure 3F-H**). The width of the lines written in the RB inks, as measured on the confocal images, is

stable at $\Omega \cong 1100\, nm$, for $\langle P \rangle \cong 160\, mW$ (**Figure 1D**), with a steep increase at the wavelength ($\cong 800\, nm$). The FWHM values are consistently lower than those written in the MB based inks, with a minimum value of the FWHM $\cong 730\, nm$ (**Figure 2D**) at <P> = 100 mW. The dependence of the FWHM on the writing power was $4.5\, nm/mW$, about half the value observed for MB inks in agreement with the fact that no temperature increase was detected from the BSA/RB ink up to <P> = 160 mW. The higher finesse of the microstructures is confirmed by SEM (**Figure 3F**) and AFM (**Figure 3G-H**) images of the L5 microstructures. Taking into account the $\cong 30\%$ shrinking of the microstructures, we can estimate form **Figure 3F** a writing spatial resolution ≅ 520-560 nm, about half that obtained in the BSA/MB inks. All these results indicate a limited influence of the localized heat load on the BSA/RB ink while writing. However, even in this case the thickness changes by about 20% at the lines crossing (**Figure 3H**).

2.1.6 Young modulus of proteinaceous micro-structures written in inks based on a anionic photo-initiator. The elastic modulus determined by AFM indentation experiments performed on rectangular parallelepiped (40μm x 40μm x 2.7μm) written in BSA/RB inks was $E_{RB} = 820 \pm 300$ kPa at [BSA] = 50 mg/mL, almost four times larger than the modulus measured in structures written in BSA/MB inks (**Figure 4A**). Moreover, the mode value of the Young modulus changes with the protein concentration (**Figure 4B**) as $E_{max} = E_0 + a[BSA]^{-p}$, with $E_0 = 83 \pm 3\, kPa$ and p = 2.9± 0.1. The parameter E_0 estimates the Young modulus of the microstructure written with no initiator. The strong power law, $p \cong 3$, indicates a high cooperativity of the cross-linking process. For a type I dye as RB, the limiting parameter is the number of dye per protein. Indeed the Young modulus increases markedly for [BSA] ≤ $100\, \frac{mg}{mL}$, when [RB]/[BSA] ≥ 1.3 (**Figure 4B**, inset).

2.3 DLW of proteinaceous microstructures containing gold Nanoparticles.

In order to build proteinaceous cross-linked microstructures incorporating photo-thermal nanoparticles, we either selected λ_{write} lying far from the nanoparticles plasmonic peak or we matched λ_{write} to the plasmonic peak, trying to exploit the local field enhancement on the nanoparticle surface to reduce the writing power.[76] The direct interaction of the photo-initiator and the nanoparticle resonances[77,78] also largely affect the photothermal efficiency of the fabricated structures.

We prepared inks containing either Gold-NanoStars (GNSs) or Gold Multi-Branched Nanoparticles (GBNPs) at 35% v/v dilution of the respective stock solution. The GNSs display two LSPR resonances,[51] at about 800nm (**Figure SI.7**), very close to the NIR wavelengths for photo-cross-linking, and at about 1200nm. The GBNPs[62] show a single LSPR resonance at about 610-630 nm, more than 100 nm away from the NIR range used to induce the photo-cross-linking. Moreover, the photothermal efficiency as measured from the Specific Absorption Rate (SAR) of the two types of nanoparticles differ by a factor $\cong 20$ (see **Figure SI.8**).

The pegylated GNSs were at first mixed to the MB ink, for which lower writing power levels were needed (**Figure 2C,D**). The pegylation of the NPs was an essential step to obtain a stable BSA/MB/GNS ink and to limit the production of microbubbles. Even with the best dispersed BSA/MB/GNS ink, we could only produce by laser direct writing at $\lambda_{write} = 780\ nm$ (scan rate $1\frac{\mu m}{s}, \langle P \rangle = 100\ mW$) wavy microstructures that were easily detaching from the glass slide upon rinsing. Increasing the power resulted only in the formation of. These findings agrees with the suggestion[78] that cationic thiazine dyes, like MB, interact with the LSPRs of the (slightly negative) gold-nanoparticles, and increase their extinction coefficient. On the contrary, the absorption peak of anionic dyes (Tin Chlorin e6, Rose Bengal and Rhodamine B) is maintained even when these dyes are in close contact with the surface of spherical gold NPs.[78]

Indeed, we found that both the GNSs and the GBNPs suffered a limited energy transfer with the RB dye, since the gold LSPR is clearly visible in the absorption spectrum of the BSA/RB/GNS ink (**Figure SI.7**). In this ink, we could fabricate regular, extended patterns at λ_{write} = 800nm, <P> = 120mW and scan rate = 10 $\mu m/s$ (see **Figure 5A1, A2**), both in the presence of GNS (BSA/RB/GNS ink) and GBNP (BSA/RB/GBNP ink). When investigated with TPE fluorescence microscopy, the microstructures free of GNS displayed a uniform emission peaked at 570 nm originating from the residual RB dye in the cross-linked structure (**Figure 5A1,** and **Figure SI.9**, green channel). An additional fluorescence signal at 440nm, due to the two-photon excitation luminescence of the gold nanoparticles,[34] was instead found on the microstructures fabricated with the inks containing the GNSs (**Figure 5A2** and **Figure SI.9**, cyan channel). On this emission channel, distinct bright spots of the size of the Point Spread Function (**Figure 5A5, Figure 5A6, Figure SI.10)** can be ascribed to single GNSs or small aggregates (**Figure 5B, Figure SI.11**). The number of particles per unit volume is 0.27 $\pm$ 0.03 particles/μm^3 (**Figure SI.11**) close to the nominal concentration of the GNSs in the fabrication ink $\cong 0.33 \pm 0.03$ particles/μm^3 . The FWHM width of the printed lines is $0.79 \pm 0.09\ \mu m$, comparable with the ones obtained without the incorporation of the gold NPs in the ink (**Figure SI.12**).

2.4 Photo-thermal activity of gold nanoparticles embedded with cross-linked BSA.

We recorded the photo-thermal activity of GNS and GBNP microstructures under irradiation of the pulsed Ti:Sapph laser at 800nm and at 760 nm, respectively. The temperature recorded with the thermo-camera on a parallelepiped ($20\ \mu m \times 20\ \mu m \times 2.7$ µm) RB/BSA/GNS microstructure increased by $\Delta T_{\omega=0} \cong 2.1 \pm 0.1\ ^oC$ in a raising time $\tau = 0.75 \pm 0.03\ s$ (see **Figure 5C**) under pulsed irradiation at $< \mathrm{P} >_{pulsed}$ = 100 mW (**Figure 5C**). The corresponding photo-thermal efficiency is (**Figure 5C**, inset) $\frac{\partial \Delta T_{\omega=0}}{\partial <P>_{pulsed}} = 20 \pm 3\ \frac{^oC}{W}$.

Very similar rising times ($\tau = 1.16 \pm 0.03\ s$), but with a lower photo-thermal efficiency, were obtained on RB/BSA/GBNP microstructures (**Figure 5D1**). The photo-thermal efficiency on the GBNPs microstructures was measured by modulating the excitation intensity with a mechanical shutter at a frequency close to the reciprocal of the growth time, $\frac{1}{\tau}$ (**Figure SI.13**). The temperature variation (extrapolated at zero modulation frequency) has a linear trend on the irradiation power (dashed line, **Figure 5D2**) with a slight round off at $\langle P \rangle > 400\ mW$ (solid line, **Figure 5D2**). The temperature increase is due to the NIR absorption GNSs in the microstructure, as confirmed by the temperature profile across the microstructure (**Figure 5D2**, inset) in the focal plane. These results (**Figure 5**) were obtained by irradiating the nanoparticles in the microstructure with a pulsed laser at an effective intensity, $< I > / \sqrt{d_c} \cong 50 - 150\ kW/cm^2$.

The temperature kinetics in BSA/RB/GNS microstructures under CW irradiation is similar (**Figure 6A**) to that observed under pulsed excitation (**Figure 5C**), with a raising time $\tau = 1.58 \pm 0.02\ s$, independent of the excitation power in the range 100 – 200 mW. The photo-thermal efficiency, $\frac{\partial \Delta T}{\partial <P>_{CW}} = 1.7 \pm 0.2\ ^oC/W$, is about ten times lower than what measured under pulsed excitation. However, the photothermal effect can be increased by raising the gold nanoparticles number in the illumination volume. In fact, on a parallelepiped approximately 100 μm thick, written in a BS/RB/GNS ink by exploiting the RB single photon absorption to induce photo-crosslinking of BSA, we measured (**Figure 6B**) a photo-thermal efficiency $\frac{\partial \Delta T}{\partial <P>_{CW}} = 12.2 \pm 0.4\ ^oC/W$, almost seven times larger than the photo-thermal effect in a proteinaceous L5 microstructure (**Figure 6A**). High resolution thermo-imaging[80] of these thicker parallelepipeds under CW excitation is shown in **Figure 6.C**.

The photo-thermal effect can be induced over an extended irradiation area. On L5 microstructures, a temperature increase of $1.1 \pm 0.05\ ^oC$ was detected over the range 0.45

$\mu m \leq \omega(z) \leq 15\ \mu m$ of the irradiation beam size (upper x-axis, **Figure 6D**) under CW laser irradiation at $\langle P \rangle_{CW}$ = 300 mW. At the same average laser power, but in pulsing mode, the maximum detected temperature raised to $7 \pm 0.06\ ^{0}C$ (**Figure 6D**, red curve), and was restricted to a thickness $\cong 4\ \mu m$, very similar to that of the microstructure.

3. Conclusions.

We have explored the possibilities and limitations to fabricate proteinaceous microstructures endowed with photothermal activity by mixing proteinaceous inks with preformed non-spherically symmetric gold nanoparticles. The most limiting parameter to this goal is the type of photo-initiators. Even though we could write stable proteinaceous microstructures in Methylene Blue based inks, we found not feasible to print photothermal structures in this ink, regardless the choice of the writing power and the high degree of stability of the nanoparticles in this ink. On the contrary, the use of Rose Bengal allowed us to write stable photo-thermal microstructures. These structures, that were obtained despite of the narrow range of writing power values available for writing in this ink, have Young modulus tunable in a wide range of values ($80 \leq E_{sample} \leq 800\ kPa$) depending on the protein/RB ratio. These values, that lie between those of tendons and cartilage,[81] indicate that the BSA/RB/GNS microstructures can be employed in tissue engineering.

Regarding the amplitude of the photo-thermal effect, we could reach on the GNS nanoparticles under focused CW excitation a photo-thermal efficiency, $\frac{\partial \Delta T}{\partial <P>_{CW}} = 1.7 \pm 0.2\ ^{o}C/W$ on thin ($\cong 3\ \mu m$) microstructures and this value raises to $\frac{\partial \Delta T}{\partial <P>_{CW}} = 12.2 \pm 0.4\ ^{o}C/W$ on 100 μm thick structures. The photo-thermal functionality obtained on the BSA/RB/GNS structures does not depend on specific interactions of the nanoparticles and the protein matrix, since also BSA/RB/GBNP microstructures display photo-thermal

functionality that are, however, $\cong 3-4$ times smaller than that of the BSA/RB/GNS microstructures, in agreement with the lower SAR of the GBNP nanoparticles. On a spot of about 15 μm radius, about the size of single cell, we could reach a temperature increase $\Delta T \cong 1.1 \pm 0.05\ ^{o}C$ from thin microstructures. These notable photo-thermal results were obtained with a gold concentration $\cong 1\%$ w/w in the microstructures, sensibly lower than what obtained by in-situ photo-synthesis of gold nanoparticles (from 3% w/w[82] to about to 20% w/w[55]). We can therefore further increase the photothermal efficiency either by increasing the thickness of the structures, as suggested by the data in **Figure 6B**, or by raising the GNS concentration in the microstructure. In fact, we could raise the GNS concentration from the present 0.27 ± 0.03 particles/μm^3 (particle-particle distance $\cong 1.5\ \mu m$) to about 10 particle/μm^3 (particle-particle distance $\cong 0.50\ \mu m$), without running into the risk of massive aggregation and plasmon delocalization among nearby nanoparticles.

All together, these results suggest that proteinaceous microstructures incorporating gold nanostars can be written in protein/Rose Bengal inks, display a tunable photothermal functionality triggered by NIR light that could be used for simultaneous physical cell treatments and observation, in order to induce and monitor cell differentiation and growing.

1

Supporting Information.
Supporting Information is available from the Wiley Online Library or from the author.

Acknowledgments: The Authors are grateful to Federico Ferrari for his precious help in the characterization of the BSA/MB microstructures and to Tiziano Catelani (University of Milano-Bicocca) for his precious help in the electron microscopy.

4. Experimental Section

Laser Direct Writing setup. The DLW setup includes (**Figure SI.1**) a Ti:Sapph femtosecond laser source (Newport, Tsunami, CA, repetition rate f_R =80MHz; pulse width $\tau_P \cong 250fs$ on the sample plane) focused by a microscope-objective (Nikon dry objective 60X, WD = 0.3 mm, NA = 0.85) on the sample that is moved by a 3-axis piezo-driven (Hera P733 coupled to a Pifoc-P725, Physik Instrument, D) stage mounted on an inverted (Nikon TE300) microscope. The piezo-actuators are controlled by an Arduino© shield (Arduino-Uno, Campustore, Italy) through a digital-to-analog converter chip that allows a maximum 50µm scanning of the sample.

Optical microscopy and confocal fluorescence imaging. The microstructures were visualized in transmission and reflection modes to check visually the quality of the washing procedure (dark regions). SRS microscopy was performed on a home made microscope for stimulated Raman spectroscopy (**Figure SI.4**). Fluorescence confocal detection was used on a Leica SP5 microscope to quantify the fluorescence emission of the PI in the fabricated structures and to measure the width of the written lines. Methylene blue (excitation $\lambda_{max} \cong$ 665nm and emission $\lambda_{max} \cong$ 692 nm) was excited at $\lambda_{exc} =$ 635nm and the emission collected on a band pass window $690 \pm 30\, nm$. Rose Bengal (excitation $\lambda_{max} \cong$ 558 nm and emission $\lambda_{max} \cong$ 572 nm) was excited at $\lambda_{exc} =$ 543 nm and the emission collected on a band pass window $580 \pm 30\, nm$.

Atomic Force Microscopy (AFM). Surface morphology (width and thickness) and elasticity of the microstructures were examined on a Nanoscope II (JPK Instruments, Berlin) AFM microscope equipped with ESP standard probe (BruckerProbes, 10-15µm tip height, average angle of the tip = 20.1 ± 2.5°) for liquid environment. Prior to each experiment, every cantilever (Nominal spring constant k = 0.2 N/m) was individually calibrated in fluid using the Thermal Noise method[83,84] in the JPK software. The elastic Young modulus of the DLW microstructures was measured by means of force – indentation curves acquired at about 70 different positions on the surface of a rectangular parallelepiped ($40\mu m \times 40\, \mu m \times 2.7\, \mu m$). The Young modulus was measured by the second order fitting of the compression force ($F(\delta)$)– indentation (δ) relation (**Figure 4A, inset**). From the fit curvature of this plot to the Hertz model function, $F(\delta) = E' \frac{tg(\alpha)}{\sqrt{2}} \delta^2$, and by assuming a tip aperture angle (four-sided pyramidal tip; $\alpha = 20^o$, producer data), we could estimate[85] the reduced Young modulus E'

which is related through the Poisson ratio of the tip (μ_{tip}) and the material (μ_{sample}) to the Young modulus of the tip, E_{tip}, according to the relation:

$$\frac{1}{E'} = \frac{1-\mu_{sample}^2}{E_{sample}} + \frac{1-\mu_{tip}^2}{E_{tip}} \quad (1)$$

Since the Silicon Nitride cantilever is very stiff ($E_{tip} \geq 100\ GPa$)[85] and the Poisson ratio $\mu_{sample}^2 \cong 0.25$,[86] the Young modulus was computed from the reduced value E' as $E_{sample} \cong E'\left(1-\mu_{sample}^2\right)$.

SEM imaging. The SEM images of the cross-linked microstructures were acquired on a Field-Emission HR-SEM Zeiss Gemini 500, at a typical volage of 5 kV.

High resolution Thermal Imaging. A focused ($\cong 30\ \mu m$) and pulsed (100 Hz) He-Ne laser spot was raster scanned on the sample while acquiring thermos-image videos. The temperature profile of each position of the laser spot was fit to a Gaussian and a synthetic image is built.[80]

BSA – Methylene Blue Ink. 300mg bovine serum albumin (Sigma-Aldrich; lyophilized, ≥96%), 6% w/w methylene blue (Sigma-Aldrich; M6900) from 4mM diluted stock solution, and 10% w/w polyvinylpyrrolidone powder (Sigma-Aldrich; MW ~ 55,000) were gently mixed, volume increased with Milli-Q water to obtain 1 mL, and kept in a fridge overnight.

BSA –Rose Bengal ink. 50mg.mL^{-1} bovine serum albumin was dissolved in a Milli-Q water. Rose Bengal (Sigma-Aldrich; dye content 95%) added to the as-prepared protein solution in a ratio to reach 2mM of concentration.

GNSs Synthesis: The GNSs were synthesized as described elsewhere.[51] They were then pegylated (PEG-SH, MW 5000) and diluted in the proteinaceous ink at 35% v/v. The GNS hydrodynamic radius is $26.5 \pm 3\ nm$ (see **Figure SI.8**) and TEM studies indicate a very regular penta-twinned planar structure with an arm length $\cong 32\ nm$ in length.[51]

GBNP synthesis. The GBNPs were synthesized by using Hepes as a reducing and stabilizing agent according to the protocol given elsewhere[62] and further pegylated with 6000 Mw thiol-PEG. The size of the GBNPs, measured by fluorescence correlation spectroscopy, is $39 \pm 4\ nm$ (**Figure SI.8**).

Thermo-imaging of the irradiated microstructures. The temperature increase was recorded on FLIR E60 thermo-camera. The Camera was set at a viewing angle of 30 degree with respect to the microscope optical axis at a distance of 40 cm. Right before starting recording the temperature profiles, the sample was dried in an ambient environment to prevent excessive temperature diffusion through the moisture layers. For the temperature measurements on the BSA/RB/GBNP microstructures, the excitation intensity was modulated by a mechanical shutter at a frequency close to $\frac{1}{\tau} \cong 1\ Hz$. The temperature signal, modulated as the same frequency as the irradiation light, was fit to a harmonic function, $\Delta T_{max}(\omega) sin\left(\omega t + \varphi(\omega)\right)$ to measure the temperature amplitude $\Delta T_{max}(\omega)$ as a function of the irradiation power. We accounted for the demodulation by correcting the bare signal, $\Delta T_{max}(\omega)$, for the Fourier band-pass function, $\Delta T_{\omega=0} = \Delta T_{max}(\omega)\sqrt{1+\omega^2\tau^2}$.

References.

[1] M. M. Nava, A. Piuma, M. Figliuzzi, I. Cattaneo, B. Bonandrini, T. Zandrini, G. Cerullo, R. Osellame, A. Remuzzi, M.T. Raimondi. *STEM CELL RESEARCH & THERAPY*. 2016, 7, 132.

[2] T. Zandrini, O. Shan, V. Parodi, G. Cerullo, M.T. Raimondi, R. Osellame. *Sci. Rep.* 2019, 9, 11761

[3] C. Sanchez, P. Belleville, M. Popall, L. Nicole, *Chem. Soc. Rev.* 2011, 40, 696.

[4] A. Baev, P.N. Prasad, H. Agren, M. Samoc, M. Wegener. *Phys. Rep.-Rev. Sec. Phys. Lett.* 2015, 594, 1.

[5] Q. Hu, C. Tuck, R. Wildman, R. Hague. In Handbook of Nanoparticles (ed. Mahmood Aliofkhazraei) 2015, 1–53 (Springer International Publishing, 2015).

[6] G. Wei, P.X. Ma. Adv. Func. Mat. 2008, 18, 3568.

[7] Y. Yagci, S. Jockusch, N.J. Turro. 2010, 43, 6245.

[8] M. Chen, M. Zhong, J.A. Johnson. *Chem. Rev.* 2016, 116, 10167.

[9] S. Maruo, J.T. Fourkas. *Laser Photon. Rev.* 2008, 2, 100.

[10] S. Maruo, S. Kawata. *J. Microelectromech. Syst.* 1998, 7, 411.

[11] V.V. Rocheva, A.V. Koroleva, A.G. Savelyev, K.V. Khaydukov, A.N. Generalova, A.V. Nechaev, A.E. Guller, V.A. Semchishen, B.N. Chichkov, E.V. Khaydukov. *Sci Rep.* 2018, 8, 3663.

[12] J. Serbin, A. Egbert, A. Ostendorf, B. N. Chichkov, R. Houbertz, G. Domann, J. Schulz, C. Cronauer, L. Fröhlich, and M. Popall Opt. Lett. 28, 301 (2003).

[13] D. Serien, H. Kawano, H., A. Miyawaki, K. Midorikawa, K. Sugioka. *Appl. Sci*. 2018, 8, 147

[14] D. Serien, K. Sugioka. *Opto-Electronic Advances* 2018, 01, 180008.

[15] J.D. Spikes, H.R. Shen, P. Kopečková, J. Kopeček. *Photochem. Photobiol.* 1999, 70, 130.

[16] B. Kaehr, J.B. Shear. *Proc Natl Acad. Sci USA* 2008, 105, 8850.

[17] W. Kaiser, C. G. B. Garrett. *Phys. Rev. Lett.* 1961, 7, 229.

[18] Y-H. Pao, P.M. Rentzepis. *Appl. Phys. Lett.* 1965, 6, 93.

[19] X. Wang, Z. Wei, C.Z. Baysah, M. Zheng, J. Xing. *RSC Advances.* 2019, 9, 34472.

[20] E.T. Ritschdorff, R. Nielson, J.B. Shear. *Lab Chip*. 2012, 12, 867.

[21] C-H. Lien, W-S. Kuo, K-C. Cho, C-Y. Lin, Y-D. Su, L. L-H. Huang, P.J. Campagnola, C.Y. Dong, S-J. Chen. *Opt. Express*, 2011, 19, 6260.

[22] R. Wollhofen, M. Axmann, P. Freudenthaler, C. Gabriel, C. Röhrl, H. Stangl, T.A. Klar, J. Jacak. *ACS Appl. Mat. & Interf.* 2018, 10, 1474.

[23] M. Malinauskas, M. Farsari, A. Piskarskas, S. Juodkazis. *Phys. Rep.-Rev. Sec. Phys. Lett.* 2013, 533, 1.

[24] S.H. Park, D.Y. Yang, K.S. Lee. *Laser Photon. Rev.* 2009, 3, 1.

[25] J. Fischer, M. Wegener. *Laser Phot. Rev*. 2013, 7, 22

[26] R. Zhang, N.B. Larsen *LAB ON A CHIP*. 2017., 17, 4273.

[27] T. Boland, T. Xu, B. Damon, X.F. Cui. Biotechnol. J. (2006) 1, 910–917.

[28] P. Delaporte, A.P. Alloncle. *Opt.Laser Technol.* 2016, 78, 33.

[29] F. Helmchen, W. Denk. *Nat Methods.* 2005, 2, 932.

[30] J-P. Fouassier, F. Morlet-Savary, J. Lalevée, X. Allonas, C. Ley. *Materials* 2010, 3, 5130.

[31] H. Tar, D.S .Esen, M. Aydin, C. Ley, N. Arsu, X. Allonas. *Macromolecules* 2013, 46, 3266.

[32] L. Chen, C. Yan, Z. Zheng. *Materials Today* 2018, 21, 38.

[33] S.T. Riahinasab, A. Keshavarz, C.N. Melton, S. Elbaradei, G.I. Warren, R.L.B. Selinger, B.J. Stokes, L.S. Hirst. *Nature Comm.* 2019, 10, 894.

[34] L. Sironi, S. Freddi, M. Caccia, P. Pozzi, L. Rossetti, P. Pallavicini, A. Donà, E. Cabrini, M. Gualtieri, I. Rivolta, A. Panariti, L. D'Alfonso, M. Collini, G. Chirico. *J. Phys. Chem. C* 2012, 116, 18407.

[35] A.B. Dahlin. Plasmonic Biosensors. IOS, Amsterdam (NL) 2012.

[36] X. Huang, S. Neretina, M. A. El-Sayed. *Adv. Mater.* 2009, 21, 4880.

[37] K.A. Willets, R.P. Van Duyne. *Annual Review of Physical Chemistry*. 2007, 58, 267.

[38] E. Boisselier, D. Astruc, *Chem. Soc. Rev.* 2009, 38, 1759−1782.

[39] N. Lee, S.H. Choi, T. Hyeon. *Adv. Mater.* 2013, 25, 2641.

[40] R.B. Smith, S. S. Gambhir. *Chem. Rev.* 2017, 117, 901.

[41] U. Saxena, A.B. Das. *Biosensors & bioelectronics* 2016, 75, 196.

[42] S. Shukla, K.T. Kim , A. Baev, Y.K. Yoon, N.M. Litchinitser, P.N. Prasad. *ACS Nano* 2010, 4, 2249.

[43] S. Shukla, E.P. Furlani, X. Vidal, M.T. Swihart, P.N. Prasad. *Adv. Mater.* 2010, 22, 3695.

[44] A. Crespi, Y. Gu, B. Ngamsom, H.J. Hoekstra, C. Dongre, M. Pollnau, R. Ramponi, H.H. van den Vlekkert, P. Watts, G. Cerullo, R. Osellame. *Lab on a Chip*. 2010, 10, 1167.

[45] G. Zhang, Q. Liao, Z. Zhang, Q. Liang, Y. Zhao, X. Zheng, Y. Zhang. *Adv. Sci.* 2016, 3, 1500257.

[46] T-T. Tsai, T-H. Huang, C-J. Chang, N. Yi-Ju Ho, Y.T. Tseng, C.F. Chen. *Sci. Rep.* 2017, 7, 3155.

[47] Pallavicini, P.; Bassi, B; Chirico, G; M. Collini, G. Dacarro, E. Fratini, P. Grisoli, M. Patrini, L. Sironi, A. Taglietti, M. Moritz, I. Sorzabal-Bellido, A. Susarrey-Arce, E. Latter, A.J. Beckett, I. A. Prior, R. Raval, Y. A. Diaz Fernandez. *Sci. Rep.* 2017, 7, 5259.

[48] C. Paviolo, P.R. Stoddart, *Nanomat.* 2017, 7, 92.

[49] G. Bodelon, C. Costas, J. Perez-Juste, I. Pastoriza-Santos, L.M.Liz-Marzán. *NANO TODAY*. 2017, 13, 40.

[50] J. Li, H. Duan, K. Pu. *Adv. Mat.* 2019, 31, 1901607.

[51] P. Pallavicini, A. Dona, A. Casu, G. Chirico, M. Collini, G. Dacarro, A. Falqui, C. Milanese, L. Sironi, A. Taglietti. *Chem. Commun.* 2013, 49, 6265.

[52] G. Palermo, T. Ritacco, D.M. Aceti, L. Pezzi, M. Giocondo, A. De Luca. *CRYSTALS*. 2017, 7, 14.

[53] W-S. Kuo, C-H. Lien, K-C. Cho, C-Y. Chang, C-Y. Lin, L.L.H. Huang, P.J. Campagnola, C.Y. Dong, S-J. Chen. *Opt. Exp.* 2010, 18, 27551.

[54] S. Shukla, X. Vidal, E.P. Furlani, M.T. Swihart, K-T. Kim, Y-K. Yoon, A. Urbas, P. N. Prasad. *ACS Nano* 2011, 5, 1947.

[55] Q. Hu, X-Z. Sun, C.D.J. Parmenter, M.W. Fay, E.F. Smith, G.A. Rance, Y. He, F. Zhang, Y. Liu, D. Irvine, C. Tuck, R. Hague, R. Wildman. *Sci. Rep.* 2017, 7, 17150.

[56] V. Tribuzi, D.S. Correa, W. Avansi, C. Ribeiro, E. Longo, C.R. Mendonca. *Opt. Express.* 2012, 20, 21107.

[57] S.A. Chechetka, M. Doi, B.P. Pichon, S. Bégin-Colin, E. Miyako. *Nanotechn.* 2016, 27, 475102.

[58] H-I. Seo, A-N. Cho, J. Jang, D-W. Kim, S-W. Cho, B.G. Chung. *NANOMEDICINE-NANOTECHNOLOGY BIOLOGY AND MEDICINE*. 2015, 11, 1861.

[59] H. Nakatsuji, T. Numata, N.S. Morone, S. Kaneko, Y. Mori, H. Imahori, T. Murakami. *ANGEWANDTE CHEMIE-INTERNATIONAL EDITION.* 2015, 54, 11725.

[60] Y. Yokoyama, M. Takeda, T. Umemoto, T. Ogushi. *Sensors and Actuators A*, 2004, 111, 123.

[61] A.N. Govyadinov, P.E. Kornilovitch, D.P. Markel, E.D. Torniainen. *Microfluid Nanofluid*. 2016, 20, 73.

[62] W. Lv, C. Gu, S. Zeng, J. Han, T. Jiang, J. Zhou. *Biosensors*. 2018, 8, 113.

[63] A.C. Balazs, T. Emrick, T.P. Russell. *Science* 2006*,* 314, 1107.

[64] J.P. Tardivo, A. Del Giglio, C. Santos de Oliveira, D. Santesso Gabrielli, H. Couto Junqueira, D.B. Tadab, S. Divinomar, R.D.F. Turchiello, M.S. Baptista. *Photodiagnosis and Photodynamic Therapy*. 2005, 2, 175.

[65] E. Niu, K.P. Ghiggino, A.W.H. Mau, W.H.F. Sasse, *J. Lumin.* 1988, 40&41, 563.

[66] E. Alarcón, A. M. Edwards, A. Aspee, F.E. Moran, C.D. Borsarelli, E.A. Lissi, D. Gonzalez-Nilo, H. Poblete, J.C. Scaiano, *Photochem Photobiol Sci.* 2010, 9, 93.

[67] P.G. Seybold, M. Gouterman, M.; Callis J. *Photochem. Photobiol.* 1969, 9, 229.

[68] J.D. Pitts, P.J. Campagnola, G.A. Epling, S.L. Goodman. *Macromolecules* 2000, 33, 1514.

[69] J. Stampf, R. Liska, A. Ovsianikov (eds). *Front Matter, in Multiphoton Lithography: Techniques, Materials and Applications*, Wiley VCH Verlag GmbH & Co. Weinheim, Germany (2016).

[70] B. Kaher, J.B. Shear *J. Am. Chem. Soc.* 2007, 129, 1904.

[71] A. Esposito, F. Federici, C. Usai, et al. *Microscopy Research and Technique*. 2004, 63, 12.

[72] M.A. Albota, C. Xu, W.W. Webb, *Appl. Opt.* 1998, 37, 7352.

[73] G.A. Blab, P.H.M. Lommerse, L. Cognet, G.S. Harms, T. Schmidt, *Chem. Phys. Lett.* 2001, 350, 71

[74] R. Akhtar, M.J. Sherratt, J.K. Cruickshank, et al. *Materials Today*, 2011, 14, 96.

[75] C. de Loubens, J. Deschamps, M. Georgelin, A. Charrier, F. Edwards-Levyc, M. Leonetti. *Soft Matter*. 2014, 10, 4561.

[76] K. Masui, S. Shoji, F. Jin, X-M. Duan, S. Kawata. *Appl Phys A*. 2012, 106, 773.

[77] A-M. Gabudean, R. Groza, D. Maniu, S. Astilean. *J. Mol. Struct.* 2014, 1073, 97.

[78] N. Narband, M. Uppal, C.W. Dunnill, G. Hyett, M. Wilson, I.P. Parkin. *Phys. Chem. Chem. Phys.* 2009, 11, 10513.

[80] M. Bouzin, M. Marini, A. Zeynali, M. Borzenkov, L. Sironi, L. D'Alfonso, F. Mingozzi, F. Granucci, P. Pallavicini, G. Chirico, M. Collini. *Nature Comm.* 2019, 10, 5523.

[81] J. Liu, H. Zheng, P.S.P. Poh, H-G. Machens, A.F. Schilling. *Int. J. Mol. Sci.* 2015, 16, 15997.

[82] Y. Liu, Q. Hu,F. Zhang, C. Tuck,D. Irvine,R. Hague, Y. He, M. Simonelli, G.A. Rance, E.F. Smith, R.D. Wildman. *Polymers*, 2016, 8, 325.

[83] J. L. Hutter, J. Bechhoefer. *Rev. Sci. Instr.* 1993, 64, 1868.

[84] R. Lévy, M. Maaloum. *Nanotechnology.* 2002, 13, 33

[85] D.C. Lin, E.K. Dimitriadis, F. Horkay. *J. Biomech. Eng.* 2007, 129, 430.

[86] A. Khan, J. Philip, P. Hess, *J. Appl. Phys.* 2004, 95, 1667.

FIGURES

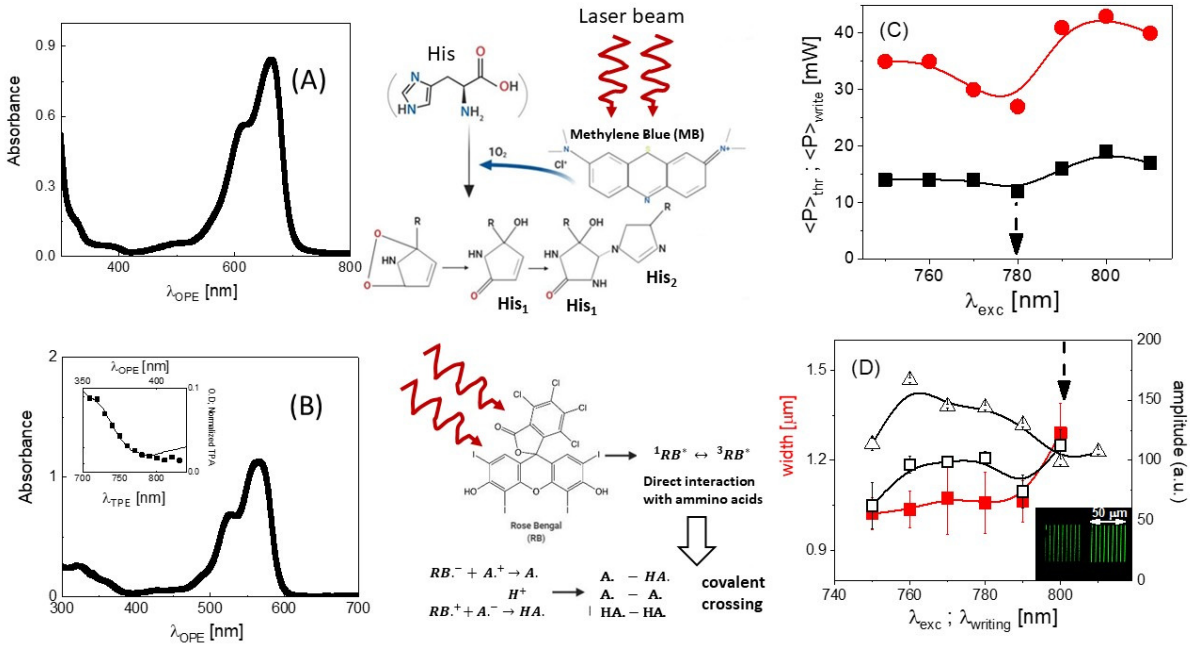

Figure 1. Panel A: absorption spectra of the MB in Milli-Q water ($\cong 12\ \mu M$). Top sketch: fundamental process of indirect [route-2; PI type II]: photo-crosslinking starts with the production of singlet oxygen by the PI. **Panel B**: RB absorption spectrum ($1\ \mu M$) in PBS buffer. The inset report a comparison of the one photon (OPE) absorption (solid line) and the two photons absorption (filled squares, from [51]). Bottom sketch: fundamental process of direct [route-1; PI type I]. The photo-activation of amino acids involves electron transfer from protein side chains producing charged amino acids ($A.^{+}/A.^{-}$) and RB ($RB.^{-}/RB.^{+}$) radicals through the RB excited triplet state. **Panel C**: dependence of the threshold, $\langle P \rangle_{\mathrm{thr}}$ (black squares), and the writing, $\langle P \rangle_{\mathrm{write}}$ (red circles), average power on the laser wavelength for a MB ink. The B-spline line is plot as a guide to the eye. **Panel D:** spatial and spectroscopic features of microstructures (inset images: structures written at $\lambda_{\mathrm{write}} = 750$ nm (left) and at $\lambda_{\mathrm{write}} = 800$ nm (right)) written in a BSA/RB ink. Left axis: FWHM width (open squares) of the lines from fluorescence confocal microscopy images (RB emission). Right axis: maximum RB fluorescence emission from the written lines (filled squares) and RB two-photon excitation spectrum (open triangles). The dashed vertical arrows indicate the writing wavelengths mostly used in this work.

Table 1. FWHM widths of L1 and L5 microstructures laser written in BSA/MB inks. All data are in micrometers; BSA concentrations are in mg/mL. All the microstructures were written at <P> = 44 mW.

		L1 structures				**L5 structures**		
Pitch[d]	[BSA]	Fluo[a]	AFM[b]	SEM[c]	Pitch[d]	Fluo[a]	AFM[b]	SEM[c]
20 (C)	300	1.14 ±0.04	1.16 ± 0.1	0.93±0.03	10 (B)	1.7±0.1	2.1±0.1	1.3±0.1
20 (C)	500	1.16 ±0.1	1.13 ± 0.08	0.86±0.04	15 (A)	1.7±0.1	2.2±0.2	1.24±0.1
5 (E)	300	1.4 ± 0.2	1.4 ± 0.2	1.25±0.07	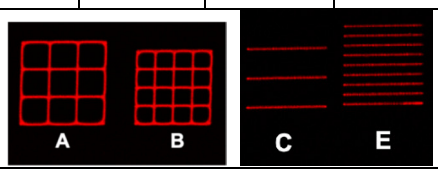			
5 (E)	500	1.16 ±0.03	1.17 ± 0.08	0.84±0.05				
			w_{Fluo}/w_{AFM}	w_{SEM}/w_{AFM}				
			1.00±0.05	0.77 ±0.03				

[a] FWHM widths measured from the fluorescence confocal images
[b] FWHM widths measured from AFM topographic images (humidified air)
[c] FWHM widths measured from SEM images
[d] length (in μm) of the full side of the square arrays or of the lines

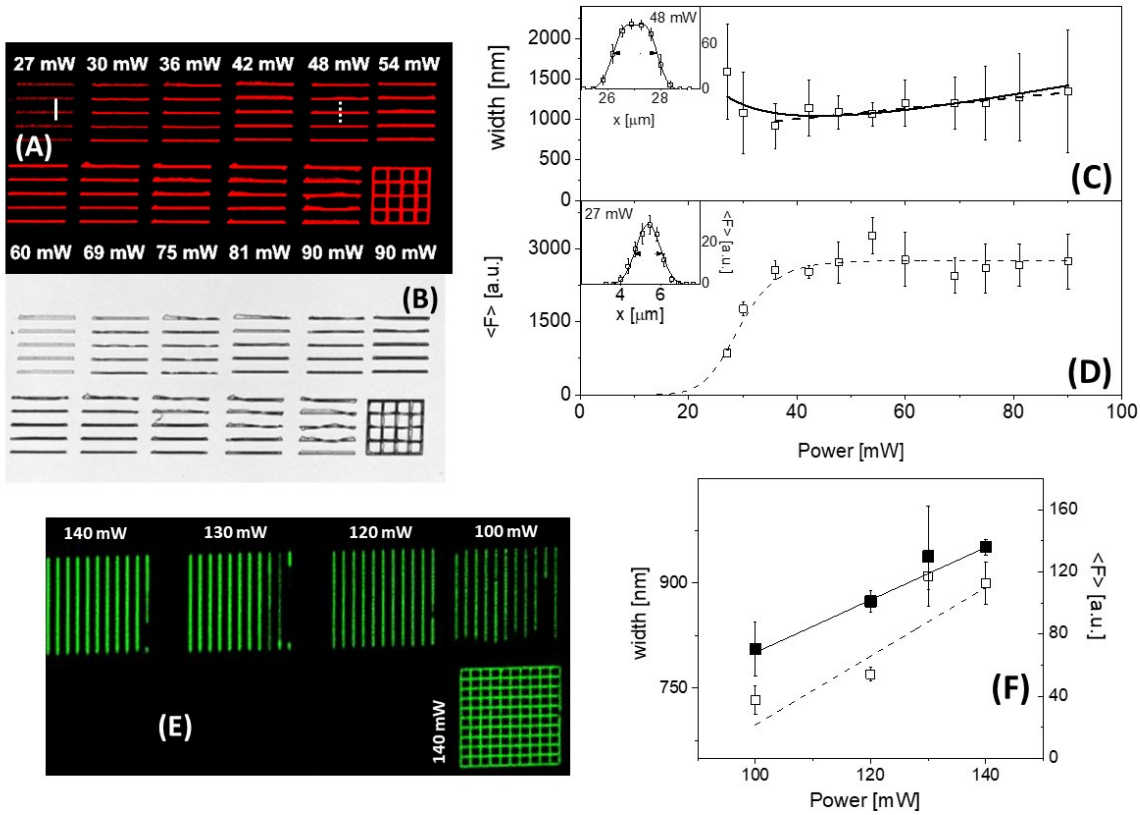

Figure 2. Effect of the NIR laser power on microstructures printed in BSA/MB (panels A-D, writing rate = 1 $\frac{\mu m}{s}$) and BSA/RB (panels E,F, writing rate = 10 $\frac{\mu m}{s}$) inks. **Panel A-D**: microstructures written on BSA/MB inks at DLW . **Panel A**: fluorescence confocal images of L1 microstructures (lines length = 40 μm) on the MB emission channel ($\lambda_{exc} = 633\ nm$, $\lambda_{em} = 665\ nm$) written at the power values listed in the figure. **Panel B**: optical transmission images of the same structures. **Panel C**: plot of the FWHM of the microstructured lines measured from panel A, as a function of the writing power at $\lambda = 780\ nm$. The lines are the fit of the data to the function $\Omega_1 + \frac{a}{\langle P \rangle^2} + b\langle P \rangle$ (solid) and the function $\Omega_0 + b\langle P \rangle$ (dashed), with the best fit parameters: $\Omega_0 = 740\ \pm 90\ nm$, $b = 7\ \pm 1.6\ nm/mW$, Ω_1=200$\pm$50 nm and $a = 0.54 \pm 0.2\ \mu m W^{-2}$. Inset: fluorescence spatial profile of the dashed line in panel A. **Panel D**: average fluorescence signal collected from the micro-structured lines as a function of the writing power. The dashed line is a fit to a sigmoidal function. Inset: fluorescence spatial profile of the solid line in panel A. **Panel E:** confocal fluorescence images of L1 microstructures (lines length = 50 μm) written at increasing laser powers (emission of RB; $\lambda_{exc} = 514\ nm$, $\lambda_{em} = 560 nm$). **Panel F:** FWHM (open squares, left axis) and average fluorescence signal (filled squares, right axis) from the images in panel E as a function of the writing power. The dashed and solid lines are best fit linear fit to the FWHM ($\Omega_0 = 200\ \pm 100\ nm$ and $b = 4.5\ \pm 2\ nm/mW$) and to the average fluorescence data.

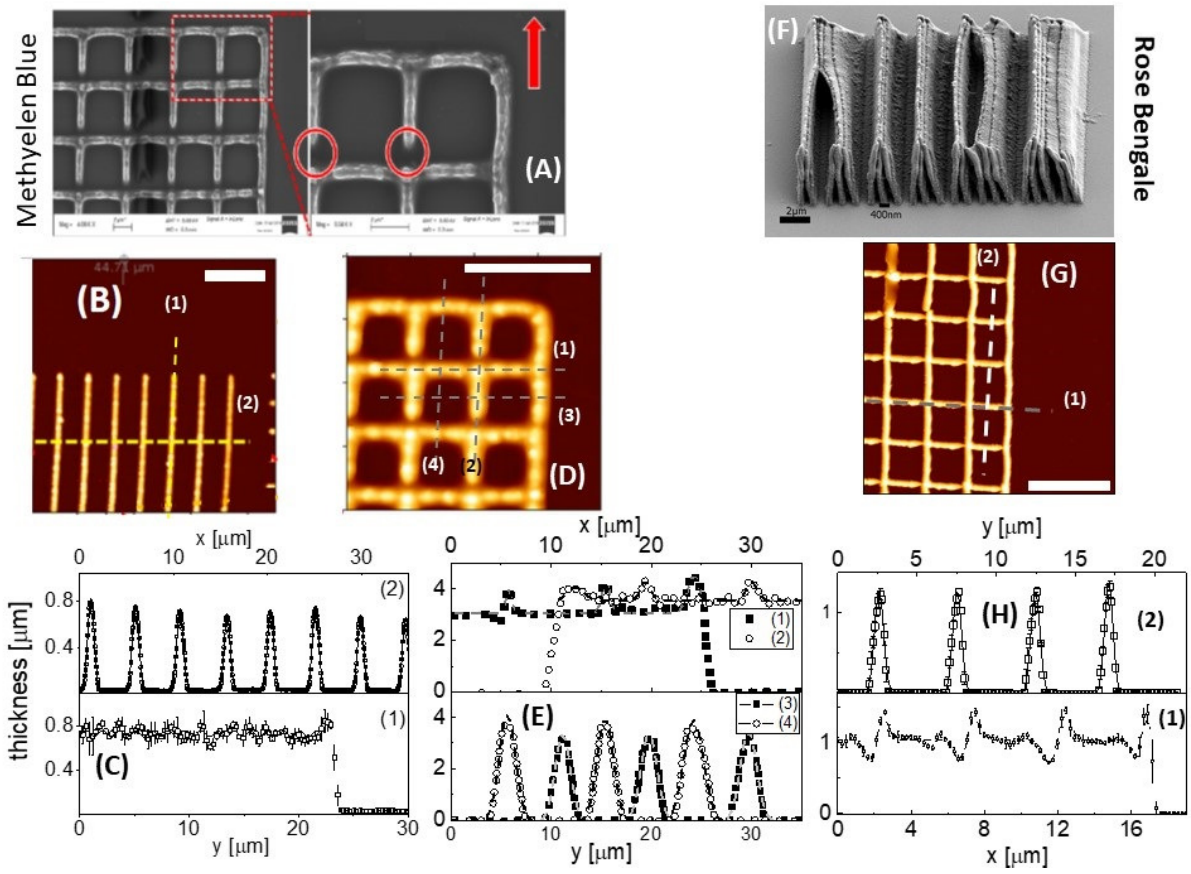

Figure *3.* SEM and AFM analysis of the L1 and L5 microstructures written in BSA/MB (**panels A-E,** <P> = 44 mW) and BSA/RB (**panels F-I**) inks. **Panel A**: SEM image of a L1 square array. The lines crossing are shown as red circles in the blow-up, where the writing direction is the red arrow. **Panel B**: AFM topographic image of a series of L1 rows. **Panel C**: profiles of sections 1 and 2 (panel B, dashed yellow lines). The solid lines are the best fit to the data with a function $t = Acos(\frac{2\pi y}{\Lambda})$ (section 1, Λ =1.5 $\pm$ 0.05 μm, A= 0.05 $\pm$ 0.006 nm) and a sum of Gaussian peaks (section 2, FWHM 0.94 $\pm$0.04 μm). **Panel D**: AFM topographic images of L5 structures. **Panel E**: profiles of the sections 1 - 4 traced in panel D. Lower panel: the dashed lines are multi-Gaussian fit to the data with FWHM = 1.87 $\pm$ 0.07 μm (trace (3)) and 2.1 $\pm$ 0.2 μm (trace (4)). Upper panel: the dashed lines are the best fit of a sum of first derivative of Gaussians to the data**. Panels F**: SEM image of a microstructure written with the BSA/RB inks ([BSA] = 50 mg/mL; [RB] = 2 mM). **Panel G**: topographic AFM image of a square array. **Panel H**: thickness profile of the structure along the dashed lines (1) and (2) in panel G. The solid line in the upper plot is the best fit of a sum of Gaussians to the data: the average FWHW of the Gaussian profiles is 660 $\pm$ 20 nm. The dashed line in the lower plot is the best fit of a sum of first derivative of Gaussians to the data (FWHM = 850 $\pm$ 220 nm). In panels B, D and G, the bar is 10 μm. In panels C, E and H, the error bars are the standard deviations computed on all the parallel horizontal or vertical lines in the structure.

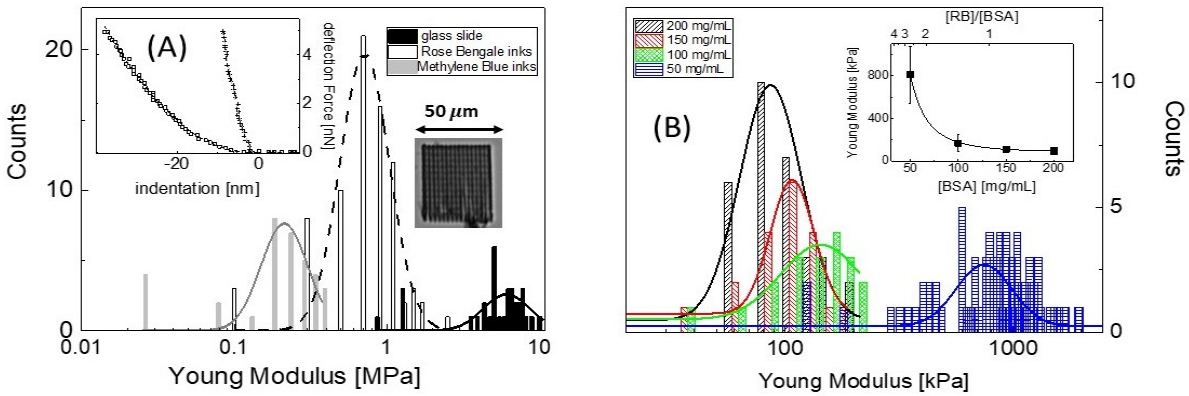

Figure 4. Young modulus of the proteinaceous microstructures measured on L5 parallelepipeds (inset image, Panel A). **Panel A**: distributions of the values of the Young modulus obtained by the Hertz model fitting of the deflection-indentation plot (inset) for the structures written in BSA/RB (open bars; [BSA] = 50mg/mL) and in BSA/RB (hatched bars; [BSA] = 300 mg/mL) inks and for the glass slide (170 nm thickness, filled bars). The black solid, black dashed and solid gray lines are best fit to log normal functions of the distributions measured on glass, on BSA/RB and on BSA/MB microstructures, respectively. The modes of the Young modulus are $E_{glass} = 6.9 \pm 2.1$ MPa, $E_{RB} = 820 \pm 300$ kPa, and $E_{MB} = 240 \pm 80$ kPa, respectively. Inset: deflection-indentation curves for glass (crosses) and MB microstructures (open squares), together with the Hertz model fit. **Panel B**: Young modulus of microstructures written in BSA/RB inks, as a function of the BSA concentration ([RB]=2mM). The distribution of the values measured for [BSA]= 50 mg/mL (blue hatch), 100 mg/mL (green hatch), 150 mg/mL (red hatch) and 300 mg/mL (black hatch) are fit to lognormal functions (solid lines). The most probable value of the Young modulus are reported in the inset together with the power law best fit: $E_{max} = E_0 + a[BSA]^{-p}$ ($E_0 = 83 \pm 3\ kPa$; p = 2.9$\pm$ 0.1).

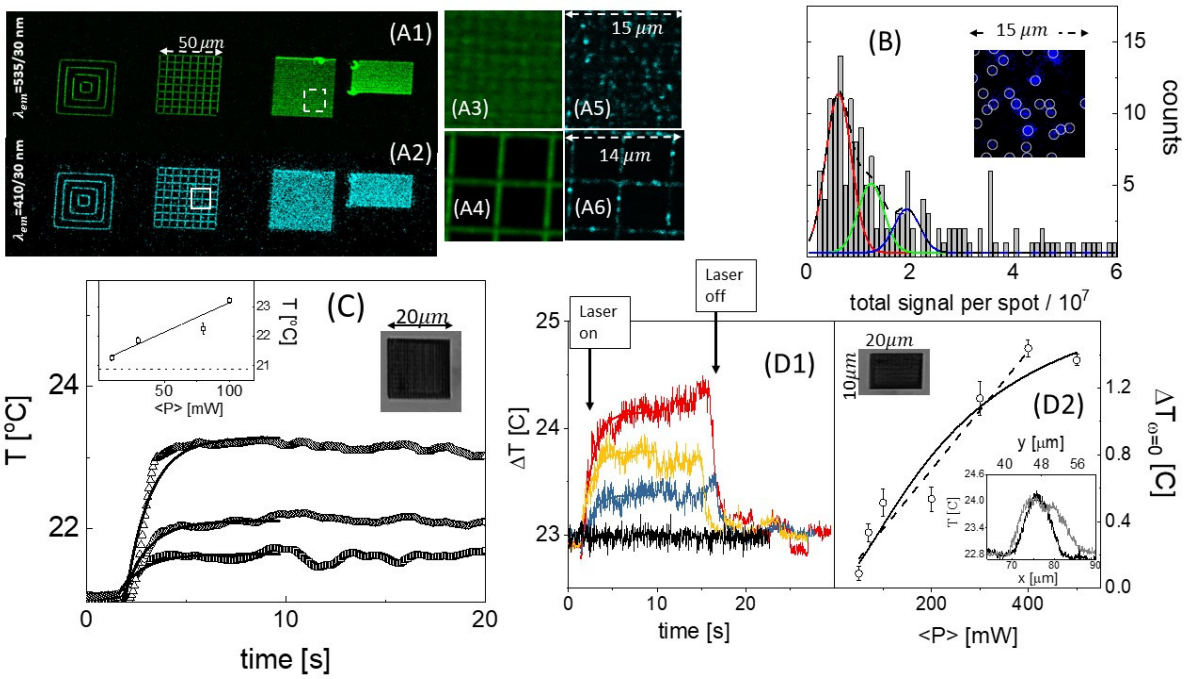

Figure 5. Two-photon fluorescence microscopy images of the microstructures written in the BSA/RB/GNS ink: the green channel (λ_{em} = 535± 20 nm) reports the RB emission (**panel A1**, 550nm) and the cyan channel reports (**panel A2**, λ_{em}= 440± 20 nm) a fraction of the two-photon luminescence emissivity of the GNSs on a 50μm X 50μm x 3.5 μm fabricated microstructures. **Panels A3, A5** and **A4, A6**: blow up (of the dashed and solid boxes, respectively) of the images in (A1) and (A2), respectively for the green (A3 and A4) and cyan channel (A5 and A6). **Panel B:** distribution of the intensity per spot measured on the GNS emission channel (panel A5). The distribution is fit to a sum of 3 Gaussian components (see SI.11). The spots where segmented as in inset image. **Panel C:** photothermal effect from branched gold nanoparticles encapsulated in proteinaceous microstructures. The temperature increase was tested on 20×20× 3 μm^3 proteinaceous BSA/MB/GNS uniform microstructures (see image inset in panel C) under continuous irradiation with the NIR pulsed laser tuned at 800nm. The temperature increase was followed in time on a thermocamera and fit to an exponential growth (solid lines) at <P> = 100 mW (squares), 80 mW (circles), 30 mW (up triangles) and 10 mW (down triangles). The limiting temperature (T_∞) as a function the average power can be fit (inset) to a linear increase: 21.1 ($\pm$0.2) + 0.02($\pm$0.003) $< P >$. **Panel D1**: temperature increase measured on BSA/RB/GBNP microstructures (20×20×1.3 μm^3 proteinaceous uniform microstructures) under continuous irradiation of pulsed laser tuned at 770 nm at<P> =100, 300 and 400 mW from bottom to top. The solid lines are a global fit of the data to an exponential growth with relaxation time $\tau = 1.16 \pm 0.03\ s$. **Panel D2**: trend of $\Delta T_{\omega=0} = \Delta T_{max}(\omega)\sqrt{1+\omega^2\tau^2}$as a function of <P>. The dashed and the solid lines are the best linear and logistic curve, respectively, to the data. The average slope is $\frac{\partial \Delta T_{\omega=0}}{\partial <P>} = 3.5 \pm 0.2\ ^oC/W$.

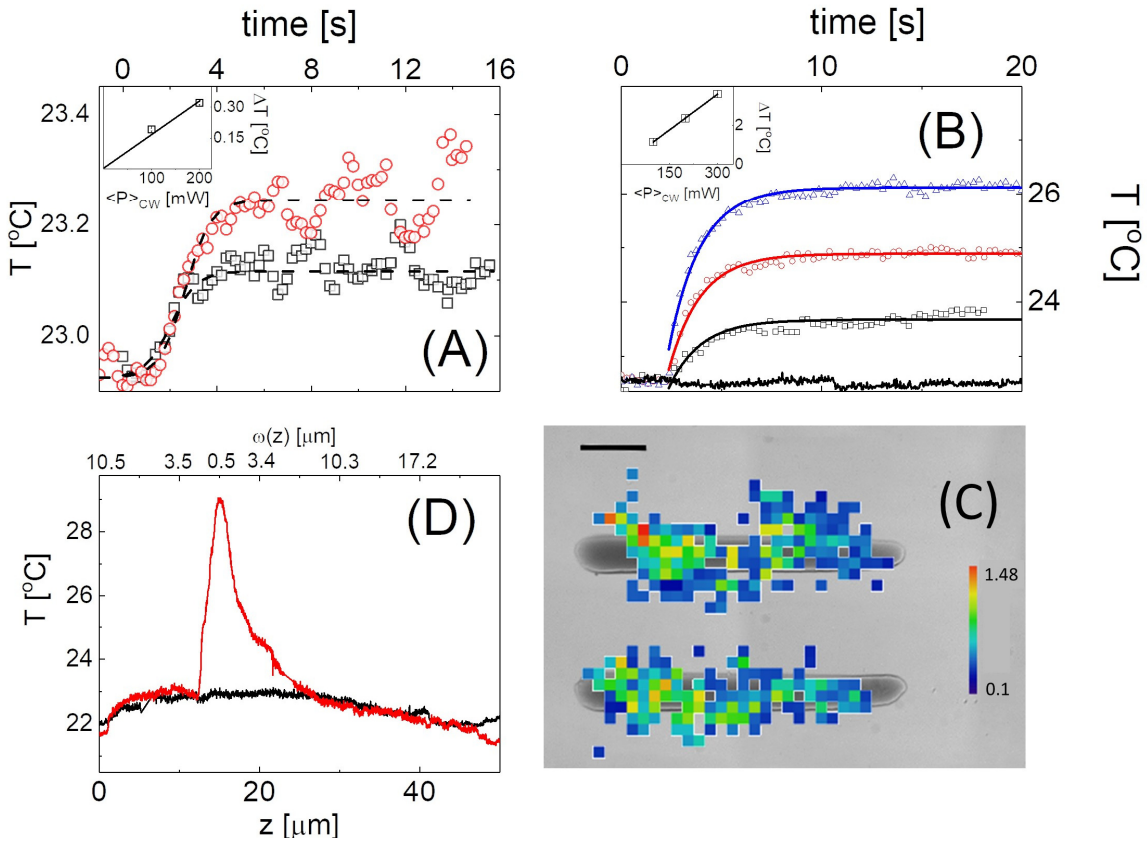

Figure 6. **Panel A**: time and power (inset) dependence of the temperature induced on the RB/BSA/GNS micro-structures by CW laser irradiation at 800 nm and $\langle P \rangle_{CW} = 100\, mW$ (black squares), $\langle P \rangle_{CW} = 200\, mW$ (red circles). The slope of the plateau temperature on the irradiation power (inset) is $1.7 \pm 0.2\ ^{o}C/W$. **Panel B:** time and power (inset) dependence of the temperature induced on the RB/BSA/GNS meso-structures ($1 \times 3 \times 0.1\, mm$) by CW irradiation at 800 nm for $\langle P \rangle_{CW} = 100\, mW$ (black squares), $\langle P \rangle_{CW} = 200\, mW$ (red circles), $\langle P \rangle_{CW} = 300\, mW$ (blue triangles). The continuous thin line is the background measured on a structure not leaded with nanoparticles. The solid lines are the best fit to an exponential growth. The slope of the plateau temperature on the irradiation power (inset) is $12.2 \pm 0.4\ ^{o}C/W$. **Panel C**: high resolution thermo-image of the structures in Panel C superimposed to their transmission image. Bar = 200 μm. All pixels with $\Delta T \leq 0.1\ ^{o}C$ were not shown. $\lambda = 633\, nm$, $\langle P \rangle_{CW} = 35\, mW$. **Panel D**: photothermal effect measured in RB/BSA/GNS micro-structures (a filled L5 square $50 \mu m$ in side, irradiation wavelength = 800 nm, <P> = 300 mW) as a function of the laser mode (CW, black; pulsed, red) and of the beam size (upper x-axis) on the micro-structured sample during a z-scan along the optical axis (lower x-axis).